Barcode Imaging Using a Light Field Camera

Xinqing Guo[1]([⊠]), Haiting Lin[1], Zhan Yu[1], and Scott McCloskey[2]

[1] University of Delaware, Newark, DE, USA
xinqing@udel.edu
[2] Honeywell ACS Labs, Minneapolis, MN, USA

Abstract. We present a method to capture sharp barcode images, using a microlens-based light field camera. Relative to standard barcode readers, which typically use fixed-focus cameras in order to reduce mechanical complexity and shutter lag, employing a light field camera significantly increases the scanner's depth of field. However, the increased computational complexity that comes with software-based focusing is a major limitation on these approaches. Whereas traditional light field rendering involves time-consuming steps intended to produce a focus stack in which all objects appear sharply-focused, a scanner only needs to produce an image of the barcode region that falls within the decoder's inherent robustness to defocus. With this in mind, we speed up image processing by segmenting the barcode region before refocus is applied. We then estimate the barcode's depth directly from the raw sensor image, using a lookup table characterizing a relationship between depth and the code's spatial frequency. Real image experiments with the Lytro camera illustrate that our system can produce a decodable image with a fraction of the computational complexity.

Keywords: Light field camera · Barcode imaging · Spatial frequency

1 Introduction

A barcode is an optical machine-readable representation of data relating to the object to which it is attached. Nowadays the ubiquitous barcodes found on product packaging significantly improve the speed and accuracy of computer data entry. A traditional 1D barcode scanner uses a line of photocells to detect the reflected light from the barcode. These linear imagers need to be well aligned with the barcode to produce accurate results and therefore the scanning process is not fully automatic. More recent 2D imagers address the automation issue by capturing the image of the entire barcode and then automatically orienting the image for decoding.

2D scanners are fundamentally low-cost cameras, and capture is limited by well-known tradeoffs between noise and blur: if the camera uses a small aperture to acquire the barcode image, the result will be corrupted by noise; if it uses a wide aperture, the result will be less noisy but the depth of field is reduced. Active illumination is used in 2D scanners using small apertures, but strict

price and power budgets typically limit this to low-power LEDs. When using wide apertures, conventionally a user would need to manually move the barcode towards or away from the scanner to ensure it is within the depth of field of the scanner. Alternatively, the scanner can conduct a focal sweep and select the proper focal slice to decode. However, implementing focal sweep requires adding moving parts to the scanner, which reduces robustness to mechanical shock. The overwhelming majority of purpose-built scanners are fixed focus for these reasons.

In this paper, we present a novel barcode scanning system by using the recent commercial light field camera. A light field camera such as Lytro and Raytrix uses a microlens array to capture multiple views of the scene in a single shot. The rich set of rays captured by the light field camera enables the user to conduct post-capture refocusing, *i.e.*, focal stack can be synthesized after the capture. This reduces the mechanical complexity of moving parts in exchange for increased computational complexity in the form of a refocusing algorithm.

The focal stack defines the extended depth of field of a light field camera. A straightforward way to utilize a light field camera for barcode scanning would be to simply apply barcode detection and decoding to images in the focal stack. However, synthesizing the complete focal stack requires applying computation-ally expensive light field rendering schemes. In order to reduce the time from capture to decoding, we present a much simpler scheme based on the frequency characteristics of barcodes. We speed up the process by first segmenting out the barcode region, which we detect from a sub-sampled version of the raw sensor image. Then, we directly estimate the depth of the barcode by analyzing the variance of pixel intensities in the lenslet images formed behind each microlens. Finally, we conduct refocusing only at the estimated depth.

Compared to 2D imagers, our system only involves two extra steps: depth estimation and barcode image rendering. With little computational cost, we gain a system with its range of depth of field nearly triples that of a conventional cam-era. Comprehensive experiments demonstrate our new light-field based barcode scanner system is fast, accurate and robust to barcode orientation, size variation, and lighting.

2   Related Work

Barcode Imaging. Recently, there has been an emerging interest on barcode reading using 2D imagers. Barcode reading consist of two distinct stages: local-ization and decoding. Tremendous efforts have been made to enhance the per-formance of both stages. Muniz *et.al.* [9] apply hough transform to the image to locate the barcode and find its optimal orientation for further decoding. Zhang *et.al.* [16] jointly analyze the texture and shape information to search for the bar-code. Chai and Hock [1] improve the barcode localization by using morphological operator to identify parallel line patterns at block level. Gallo and Manduchi [5] employ a deformable template matching method and enforce global spatial coherence to correctly read barcodes in difficult situations. Xu and McCloskey

[14] describe a system for localizing and deblurring motion-blurred image using a flutter shutter camera. In contrast to their methods, our system features a better light efficiency and aims at reducing the defocus blur of the barcode image.

Light Field Photography and Depth Estimation. Integral or light field photography captures a rich set of rays to describe the visual appearance of the scene. A distinct advantage of light field photography is the ability to render an image after exposure with a desired focal plane. Modern light field rendering is introduced by Levoy and Hanrahan [8] and Gortler *et.al.* [7]. Early approaches [12] utilize camera arrays to capture a light field with high spatial resolution. However, the system tends to be bulky and impractical for daily use. Ng [10] designs a hand-held light field camera where a microlens array is placed on top of the sensor to optically sort the rays by direction onto the pixels underneath. In addition to its refocusing capability, light field is also applicable to depth estimation. Several methods [2,13] exploit the epipolar-plane image (EPI) to extract the disparity map. Others use correspondences [4] or combined with depth from defocus technique [11] to achieve similar result. In contrast to their methods for general scenes which are geometrically complex, our work focuses on barcode imaging and only extract the depth of barcode region based on its unique frequency characteristics, thus largely reducing the computational cost. Similarly, our rendering approach also prefer speed to quality. We utilize basic ray tracing for rendering a correct image, without using other image enhancement techniques such as [4] since they won't benefit barcode decoding. In this paper, we use Lytro camera to validate our algorithm, but note that our methods apply to most microlens-based light field camera.

3 Frequency Characteristics

Conventional barcodes are composed of high contrast black and white bars or patches, which facilitate the localization process. Several approaches have been proposed and optimized to take advantage of the texture information for localization. However, the imaging mechanism of light field camera will distort and deteriorate these features, making existing approaches less effective, even unusable. The structure of light field camera is similar to a conventional camera, except that it adds a microlens array in front of the sensor to further diverge the rays based on their directions. Thus, the resultant raw light field image consists of hundreds of thousands of lenslet images, as shown in Fig. 1. Directly locating the barcode on the raw light field image would be extremely challenging: each lenslet image contains at most 10×10 pixels; and the high contrast in the boundary region of each lenslet image will fail gradient based detection algorithms.
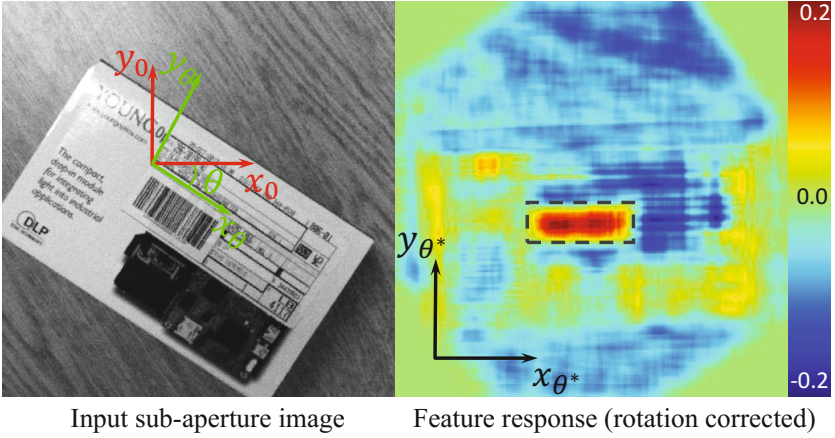
3.1 Barcode Localization

In order to address these issues, we aim to first localize the barcode on a sub-aperture image instead of the raw image. A sub-aperture image is a normal
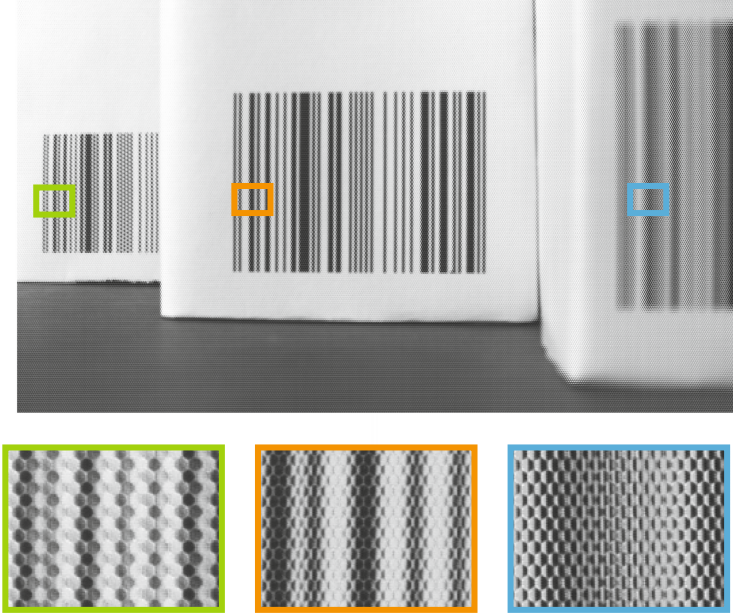
Fig. 1. Lenslet image pattern changes with the depth of the barcode

2D image composed by stitching together the same pixels underneath each microlens. It can be thought of as an image taken by a virtual camera with its center of projection in front of the main lens. In our case, we pre-calibrate the center of each lenslet image and pick the center pixels to generate a central sub-aperture image. Interpolation is required since the lenslet arrangement is hexagonal.

Although the sub-aperture image is of low resolution (about 328×378 for Lytro) which inhibits direct decoding, it is detailed enough for barcode localization. We extend the method proposed in [5] by incorporating the barcode orientation into the feature computation, and analyse the shape of the region with high average feature responses for robust localization. For each angle $\theta \in \{-90, -85, ..., 90\}$, feature response $I_e^\theta(p) = |I_{x_\theta}(p)| - |I_{y_\theta}(p)|$ is evaluated at each pixel p, where $I_{x_\theta}(p)$ and $I_{y_\theta}(p)$ are the image gradient along orthogonal directions $x_\theta(\cos\theta, \sin\theta)$ and $y_\theta(-\sin\theta, \cos\theta)$ respectively. A box filter is applied to I_e^θ to get locally averaged feature response $\bar{I}_e^\theta$. The potential barcode region is identified by a connected region of constantly high average response $\bar{I}_e^{\theta^*}$ with θ^* maximizing the mean of $\bar{I}_e^\theta(p)$'s within the region. The shape of this region is also required to be tightly bounded by an oriented rectangle. Within this rectangle, we compute the size of the candidate barcode as the distance between the first and the last black bars. In order to eliminate the effects of illumination variations, the input sub-aperture image is preprocessed using local histogram equalization. Fig. 2 shows an example of our barcode localization algorithm.

| | |
| Input sub-aperture image | Feature response (rotation corrected) |

Fig. 2. A barcode localization example. An optimal rotation angle θ^* is determined maximizing the mean feature response of the potential barcode region.

Note that our localization method is designed for 1D barcode. We refer the reader to [14] and other related work for 2D barcode localization. After we locate the barcode in the sub-aperture image, we can continue to crop the corresponding barcode region in the raw light field image and only process this region to speed up our following ray tracing algorithm.

3.2 Spatial Frequency *vs.* Depth

We first study the correlation between the spatial frequency of the raw barcode region and its depth. Here we assume that the barcode is approximately frontal parallel to the camera so we only consider one depth value. As shown in Fig. 1, barcodes positioned at different depth exhibits different lenslet image patterns. In the first inset, each lenslet image shows uniform color, indicating the image plane of the main lens coincides with the plane of the microlens array. As the barcode moves nearer to the camera, increasing intensity variations are evident in lenslet images. Therefore, our intuition is to use this statistical characteristics of barcode for depth estimation.

To better illustrate our algorithm, we simplify the barcode as evenly distributed black and white bars. The spatial frequency of the barcode is defined as the number of line pairs per unit length. Fig. 3 shows two cases of formation of lenslet images. In the first case, the image plane of main lens falls in front of the microlens array, where each lenslet image is a real image. On the contrary, when the image plane is behind the microlens array, a virtual image will be observed. Given the spatial frequency of the barcode X_1, we apply thin lens equation to compute the spatial frequency at the image plane of the main lens X_2 as:

$$X_2 = \frac{a}{b} \cdot X_1 = \frac{a-F}{F} \cdot X_1 \tag{1}$$
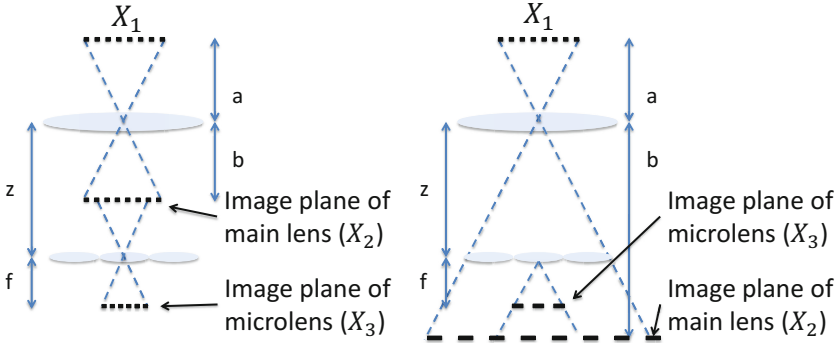
Fig. 3. Spatial frequencies of the barcode image at different image planes

where a is the object distance and F is the focal length of the main lens. We repeat this process to obtain the spatial frequency of the barcode image at the sensor plane X_3 as:

$$X_3 = \frac{z - b}{f} \cdot X_2 = \frac{a(z - F) - zF}{Ff} \cdot X_1 \qquad (2)$$

when the main lens image plane is in front of the microlens and

$$X_3 = \frac{z - b}{f} \cdot X_2 = \frac{a(F - z) + zF}{Ff} \cdot X_1 \qquad (3)$$

when the image plane is behind the microlens. Here z represents the distance between the main lens and the microlens, b is the image distance and f is the focal length of the microlens. In both cases a linear relationship between the barcode's spatial frequency at the sensor and its depth can be observed.

3.3 Variance *vs.* Depth

Although we can mathematically compute the sensor plane's spatial frequency X_3, it is very challenging to robustly measure this frequency since each lenslet image is only of size 10×10 pixels–*i.e.* a very small portion of the barcode, with its boundary region corrupted by vignetting. In our experiments, we observe at most two color transitions inside each lenslet image. Therefore, we instead use variance to represent the spatial frequency of each lenslet image. Specifically, we define a window around each lenslet center and measure the variance of pixel intensities within the window. Our intuition is that the higher the spatial frequency, the larger the chance to observe intensity transitions inside the window. We then compute the overall variance as the spatial frequency measurement by averaging the variances from the lenslet images inside the barcode region.

To formulate the correlation between variance and depth, we make following assumptions based on observation that at most two intensity transitions appear
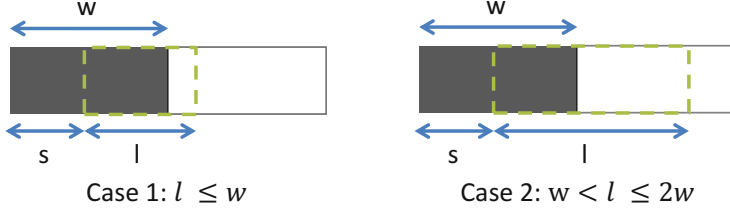
Fig. 4. Lenslet images function as a sliding window across the barcode region

within each lenslet image. Next, we regard the light field camera as a relay imaging system, which consist of mainlens and microlenses as pinhole cameras. We first analyze the image captured by the microlens, then extend our analysis to the whole system.

First we want to define variance σ^2. Suppose our target is evenly distributed black/white bars. Our pinhole camera has N pixels and the captured image contains m white pixels and n black pixels. And we further denote the intensity of the white pixel as 1 and that of black pixel as 0. Then we can get

$$\mu = \frac{m}{m+n} \tag{4}$$

$$\sigma^2 = \frac{1}{N}\sum_{i=1}^{N}(x_i - \mu)^2 = \frac{mn}{(m+n)^2} \tag{5}$$

where μ is the mean value of the image and x_i is the pixel value.

Next we only consider the lenslet image. As each lenslet image only observes a very small portion of the barcode, its variance changes with its relative positions with the bar. As shown in Fig. 4, we denote the bar width of the image as w, the sensor size at the barcode image plane as l and the distance between the starting point of the lenslet image and a intensity transition as s. Then we continue our analysis in two cases:1) If $l \leq w$, then

$$\sigma^2 = \begin{cases} 0, & s \leq w-l \\ \frac{-s^2+(2w-l)s+lw-w^2}{l^2}, & w-l < s \leq w \end{cases} \tag{6}$$

We only compute the variance σ^2 as a function of s ranging from 0 to w because it is a periodic function. Since the lenslets are hexagonally arranged, their images can be considered as a sliding windows across the entire barcode image. From the distribution of σ^2, we can get the average variance $\bar{\sigma}^2$ as:

$$\bar{\sigma}^2 = \frac{\int_0^w \sigma^2 ds}{w} = \frac{1}{w}\left(\int_0^{w-l} \sigma^2 ds + \int_{w-l}^{w} \sigma^2 ds\right) = \frac{l}{6w} \tag{7}$$

It is evident that average variance $\bar{\sigma}^2$ is linearly relates to l. We can further map l through the mainlens to the real barcode as L. By using similar triangles, we

have $L = \frac{al}{b} = \frac{A}{Ff}[(z-F)a - zF]$ or $\frac{A}{Ff}[(F-z)a + zF]$ and $l = \frac{A(z - \frac{aF}{a-F})}{f}$, where A is the size of the sensor and a, b, F, f, z are defined in last section. Therefore, each lenslet image covers an area of l on the barcode image through mainlens, and an area of L on the real barcode. Because l increases monotonically with the increase of a, we can obtain a one-on-one mapping between the depth a and average variance $\bar{\sigma}^2$.

2) if $w < l \le 2w$, we have

$$\sigma^2 = \begin{cases} \frac{-s^2 + (2w-l)s + lw - w^2}{l^2}, & 0 < s \le 2w - l \\ \frac{lw - w^2}{l^2}, & 2w - l < s \le w \end{cases} \quad (8)$$

Similarly, we compute its average variance $\bar{\sigma}^2$ as:

$$\bar{\sigma}^2 = \frac{\int_0^w \sigma^2 ds}{w} = \frac{1}{w}\left(\int_0^{2w-l} \sigma^2 ds + \int_{2w-l}^w \sigma^2 ds\right) = \frac{w^2}{3}l^{-2} - \frac{1}{6w}l - wl^{-1} + 1 \quad (9)$$

To prove $\bar{\sigma}^2$ monotonically increases with l, we compute its first and second order derivative as $(\bar{\sigma}^2)' = -\frac{2w^2}{3}l^{-3} - \frac{1}{6w} + wl^{-2}$ and $(\bar{\sigma}^2)'' = 2w^2 - 3wl$. Since $w < l \le 2w$, $(\bar{\sigma}^2)'' < 0$. We further examine the value of $(\bar{\sigma}^2)'$ at $l = w$ and $l = 2w$, they are both larger than 0. Therefore, we can prove that $(\bar{\sigma}^2)' > 0$, so $\bar{\sigma}^2$ monotonically increases with l. Similar to the first case, we can also obtain a one-to-one mapping between the depth and average variance.

4   Efficient Refocusing

Our analysis above reveals that we can quickly use the variance to determine the depth of the barcode. This allows us to conduct refocusing with high efficiency.

4.1   Barcode Depth Estimation

To validate our use of variance as a depth cue, we measure the average variance of several randomly selected UPC-A barcodes over a range of distances from the camera. Fig. 5(a) shows the average results using different window sizes for variance computation. Clearly we can see valley shaped curves with two approximately linear regions. The bottom of the curve indicates the main lens image plane falls on the microlens, so the lenslet image gets uniform intensity which results in a minimum overall variance. Here one variance value may correspond to two different depths. To resolve this two-fold ambiguity, we only use the left linear region in our experiments, as barcodes of practical sizes at depths in the right linear side are resolution limited even when properly focused. If necessary, the right linear side can be used similarly to estimate another depth in the case that the depth from the left side leads to a undecodable result. Note that due to defocus blur and resolution limitation [6] in the lenslet image, the curve fluctuates in both ends, making these regions unusable. For robustness reasons, we estimate three depth values independently based on different window sizes 3×3, 5×5 and 7×7, and compute the mean of the corresponding depths as the final estimation.
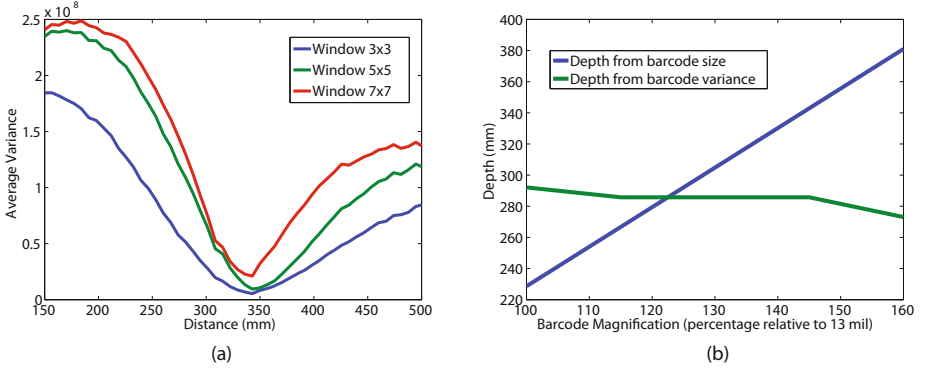
Fig. 5. (a) The average variances of the barcode image using different window sizes *vs.* its depth. (b) The depth of the barcode region is determined jointly by the variance and the size of the detected barcode region.

The variance *vs.* depth curve in Fig. 5(a) is for standard 13 mil barcodes. Scaling the size of the overall barcode will change the underlying spatial frequency X_1, and change the relationship between depth and variance. This is inevitable since product manufacturers tend to adjust the size of the barcode to suit the package. Our solution is first to build a look-up table indexed by variances per barcode size. Then we jointly determine the final depth based on both the variance and the size of the detected barcode region in the central sub-aperture image. From projective geometry, we obtain the relationship between the barcode image size s and the depth d as $s \propto S/d$, where S is the original size of the barcode. Fig. 5(b) illustrates our depth determination strategy. Given a detected barcode size, the larger the barcode's original size, the further its distance. Given a measured variance, another size *vs.* depth curve is formed by collecting depths from the look-up tables for corresponding barcode sizes. The ground truth original barcode size and the depth are therefore indicated by the intersection of these two lines/curves.

4.2 Refocusing

The final step in our light field barcode imaging system renders a focused image of the barcode region, using the depth estimated from the variance and size of this region. We set out to perform ray tracing to generate the in focus barcode image. Ray tracing mimics the physical process of image formation. The intensity of a point on the target image plane (virtual plane) is computed by integrating all the rays of different directions passing through it.

As shown in Fig. 6(a), adopting two parallel plane parameterization (2PP) [8], a ray can be indexed by $(\mathbf{s}, \mathbf{u})$, where $\mathbf{s}$ and $\mathbf{u}$ are the 2D intersections with the target image plane $\Pi_{\mathbf{s}}$ and the microlens plane $\Pi_{\mathbf{u}}$ respectively. The formation process of the target image I' can be summarized as:

(a) Ray tracing   (b) Results of ray tracing and Shift-and-add
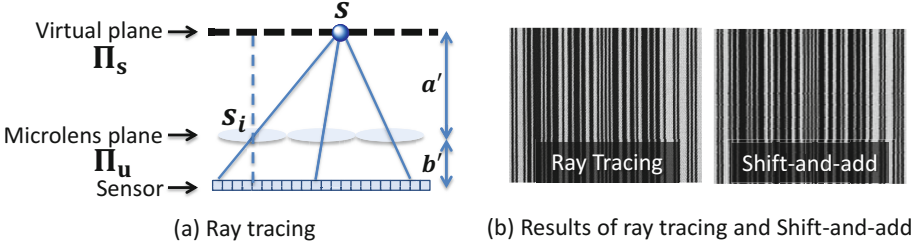
Fig. 6. (a)High quality barcode rendering by ray tracing. (b)Results from two implementations of refocusing algorithm.

$$I'(\mathbf{s}) = \int r(\mathbf{s}, \mathbf{u}) d\mathbf{u}, \tag{10}$$

where $r(\mathbf{s}, \mathbf{u})$ is the irradiance of the corresponding ray and is recorded by the sensor. As shown in the Fig. 6(a), the directions of the rays are discretized through the lenslets. Let $\mathbf{s}_i$ denote the location of the optical center of lenslet m_i, a' the distance from $\Pi_\mathbf{s}$ to $\Pi_\mathbf{u}$ and b' the distance from $\Pi_\mathbf{u}$ to the sensor plane, Eq. 10 can be rewritten discretely as:

$$I'(\mathbf{s}) = \sum_i I((\mathbf{s}_i - \mathbf{s})\frac{b'}{a'} + \mathbf{s}_i), \tag{11}$$

where I is the raw image on the sensor.

In our experiments, we first adopt the method proposed by [3] and use preloaded white images from Lytro camera to locate the lenslet centers $\mathbf{s}_i$ according to the camera's focal length setting. The target image plane is then determined based on the estimated depth and is discretized into pixels. Next we conduct ray tracing for each pixel $\mathbf{s}$ to gather the recorded irradiance of the rays and apply bilinear interpolation to achieve a better approximation of the pixel value. Note that there is a tradeoff between the resolution of the barcode image and its computational cost. The ray tracing technique provides the flexibility to vary the resolution by simply changing the sampling rate on the virtual plane. In our experiments, we render a barcode image of approximately 200×200 pixels to balance these two factors. Compared to the shift-and-add refocusing algorithm in [10], which requires rectified light field images (lenslet images arranged on grids), our method produces sharper rendering results as shown in Fig. 6(b). The blur artifacts in the shift-and-add result is due to the interpolation operation conducted when generating the rectified light field image from Lytro data. Generating images with even higher quality is still possible [13,15], but impractical due to its high computational cost.

5   Experiments

We use Lytro camera as our prototype light field camera. The raw images are preprocessed according to the metadata from Lytro's proprietary file format [3]
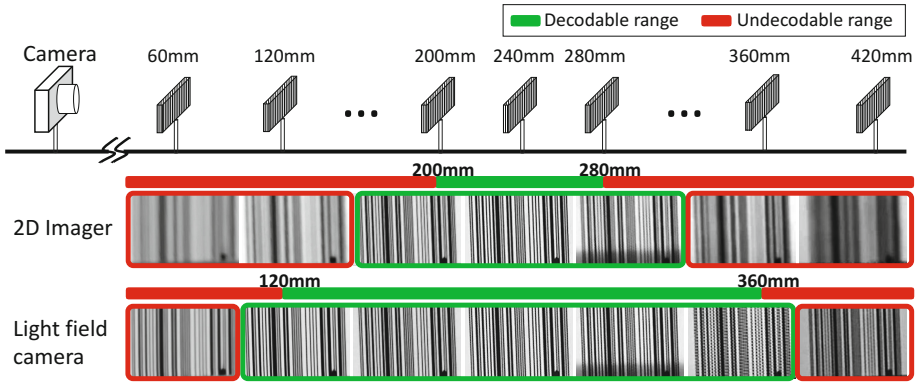
Fig. 7. Barcode images captured at variant depths using different devices. Light field camera largely extends the decodable range while keeping the noise level low.

and the vegnetting effects are removed using the pre-stored calibration images in Lytro camera. Demosaicing is then applied to get the final raw light field image. While capturing, we keep both the focal length and focal plane unchanged to simulate a light field camera without active parts.

Depth of Field. Our first experiment is to determine the amount of extended depth of field the light field camera has over a conventional camera. We collect a set of images of the barcode positioned at 60 mm to 420 mm from the camera with a incremental step of 6.9 mm. Using Lytro's desktop application, we generate two groups of images using the same focal length and aperture size: 1) one with focal plane coincides with the moving barcode and 2) the other one with a fixed focal plane simulating the conventional scanner. We test the decodability of the barcode images with a proprietary decoder. Results show that images from conventional camera is only decodable within a range of 80 mm due to the defocus blur. On the contrary, the images from light field camera features extended depth of field, with a decodable region of 240 mm, which nearly triples the range of conventional camera. Fig. 7 shows the comparison of the decodable range of 2D scanner and the light field camera, as well as the sharpness of their resultant images.

Depth Estimation and Image Rendering. Our subsequent experiments are to validate our barcode localization and depth estimation algorithm. We set our recognition target to be the standard 13 mil UPC-A barcode with 1.0x, 1.15x, 1.3x, 1.45x and 1.6x magnifications. Our variance *vs.* depth look up tables and size *vs.* depth curves are calibrated based on training data of random UPC-A codes. Barcodes with codes different from the training data are used for test. Fig. 8 shows the comparison between the estimated depths and the ground truth depths for barcodes of different sizes. The estimation errors are less than 50 mm which is within the decodable range. Fig. 9 shows our rendering results for barcodes on real products. Note that our algorithm is robust to different
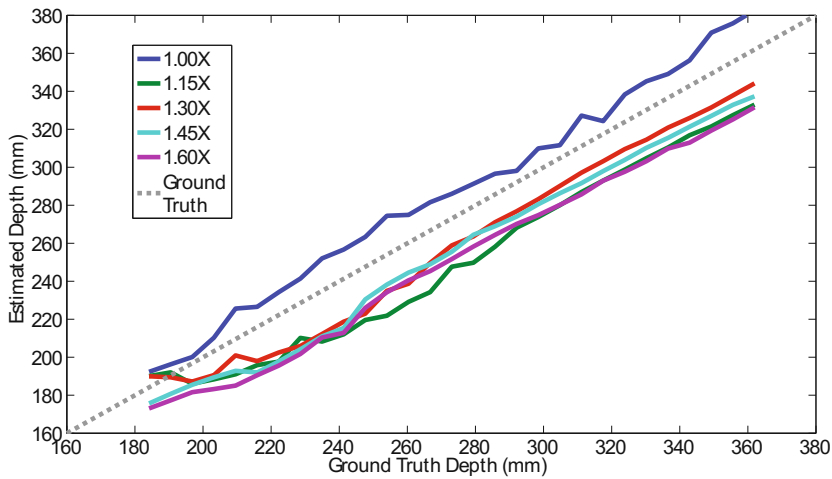
Fig. 8. Comparison between measured depths and the ground truth depths for barcodes of different sizes
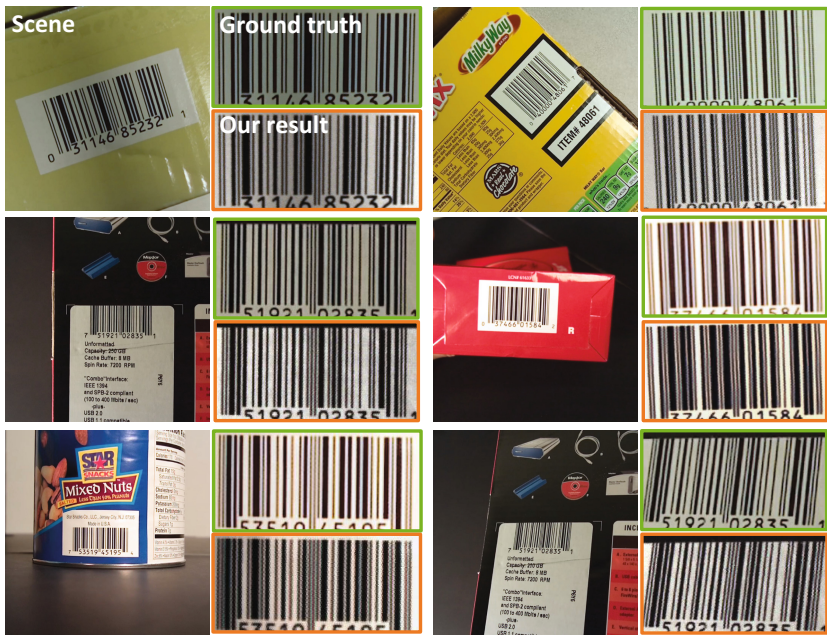
Fig. 9. Rendering results of real barcodes using our scanning system. The full image on the left of each barcode example is the in focus image at the ground truth depth. Our rendering results are shown with orange boundary, while the ground truth are shown with green boundary for comparison.

sizes, orientations and nonuniform lighting conditions. Although we assume the barcode is approximately frontal parallel to the camera, our algorithm is tolerant

Fig. 10. An example where our algorithm fails

of slight projective distortion as shown in the last example in Fig. 9. However severe distortions result in failure cases as shown in Fig. 10. The main reason for this failure case is that our barcode localization algorithm detects a rectangle rather than a tight parallelogram only encloses the barcode. The non-barcode region inside our rectangle pollutes the variance estimation for depth estimation.

Running Time. We compare the processing speed/time of our system and a 2D scanner. A 2D scanner directly locates and decodes the barcode after exposure, while our system requires two extra steps: depth estimation and rendering of the barcode region. In our C++ implementation, the extra steps take around 0.2s for each light field image. Note that the result is not fully optimized. With application-specific integrated circuit (ASIC), as is implemented in most scanners, the overall processing time can be further reduced.

6   Conclusions and Future Work

In this paper, we present a novel, extended depth of field barcode scanning system based on a commercial light field camera. While a purpose-built light field scanner would likely use a smaller aperture than the Lytro camera, our emphasis has been on algorithmic improvements that would apply to such hardware. Our efficient, high quality barcode image rendering technique first segments the barcode and then estimates its depth in order to render only the necessary focal slice. The depth estimation is based on the spatial frequency and the size of barcode region, and is implemented by employing calibrated look up tables. Real barcode imaging experiments demonstrate the effectiveness of our scanning system. Depending on the size of the barcode in the image, and on the depth complexity of the scene, these improvements can dramatically reduce the amount of time needed to produce a decodable image. We will extend our system to 2D barcode scanning for our future work.

References

1. Chai, D., Hock, F.: Locating and decoding ean-13 barcodes from images captured by digital cameras. In: 2005 Fifth International Conference on Information, Communications and Signal Processing, pp. 1595–1599 (2005)
2. Dansereau, D., Bruton, L.: Gradient-based depth estimation from 4d light fields. In: Proceedings of the 2004 International Symposium on Circuits and Systems ISCAS 2004, vol. 3, pp. 549–552 (2004)
3. Dansereau, D., Pizarro, O., Williams, S.: Decoding, calibration and rectification for lenselet-based plenoptic cameras. In: 2013 IEEE Conference on Computer Vision and Pattern Recognition (CVPR), pp. 1027–1034 (2013)
4. Fiss, J., Curless, B., Szeliski, R.: Refocusing plenoptic images using depth-adaptive splatting. In: International Conference on Computational Photography (ICCP 2014). IEEE Computer Society (2014)
5. Gallo, O., Manduchi, R.: Reading 1d barcodes with mobile phones using deformable templates. IEEE Transactions on Pattern Analysis and Machine Intelligence **33**(9), 1834–1843 (2011)
6. Georgiev, T., Yu, Z., Lumsdaine, A., Goma, S.: Lytro camera technology: theory, algorithms, performance analysis. In: Proc. SPIE 8667 (2013)
7. Gortler, S.J., Grzeszczuk, R., Szeliski, R., Cohen, M.F.: The lumigraph. In: SIGGRAPH 1996, pp. 43–54 (1996)
8. Levoy, M., Hanrahan, P.: Light field rendering. In: SIGGRAPH 1996, pp. 31–42 (1996)
9. Muniz, R., Junco, L., Otero, A.: A robust software barcode reader using the hough transform. In: Proceedings of the 1999 International Conference on Information Intelligence and Systems, pp. 313–319 (1999)
10. Ng, R., Levoy, M., Bredif, M., Duval, G., Horowitz, M., Hanrahan, P.: Light field photography with a hand-held plenoptic camera. Stanford University Computer Science Tech. Report **2**, 1–11 (2005)
11. Tao, M.W., Hadap, S., Malik, J., Ramamoorthi, R.: Depth from combining defocus and correspondence using light-field cameras. In: Proceedings of the 2013 IEEE International Conference on Computer Vision, pp. 673–680 (2013)
12. Vaish, V., Wilburn, B., Joshi, N., Levoy, M.: Using plane + parallax for calibrating dense camera arrays. In: 2004 IEEE Conference on Computer Vision and Pattern Recognition (CVPR), pp. 2–9 (2004)
13. Wanner, S., Goldluecke, B.: Variational light field analysis for disparity estimation and super-resolution. IEEE Transactions on Pattern Analysis and Machine Intelligence **36**(3), 606–619 (2014)
14. Xu, W., McCloskey, S.: 2d barcode localization and motion deblurring using a flutter shutter camera. In: 2011 IEEE Workshop on Applications of Computer Vision (WACV), pp. 159–165 (2011)
15. Yu, Z., Guo, X., Ling, H., Lumsdaine, A., Yu, J.: Line assisted light field triangulation and stereo matching. In: Proceedings of the 2013 IEEE International Conference on Computer Vision, pp. 2792–2799. ICCV 2013 (2013)
16. Zhang, C., Wang, J., Han, S., Yi, M., Zhang, Z.: Automatic real-time barcode localization in complex scenes. In: 2006 IEEE International Conference on Image Processing, pp. 497–500 (2006)